01 Dec 1998

An Image Model based on Occluding Object Images and Maximum Entropy

John A. Stuller
Missouri University of Science and Technology, stuller@mst.edu

Rahul Shah

Recommended Citation

J. A. Stuller and R. Shah, "An Image Model based on Occluding Object Images and Maximum Entropy," *IEEE Transactions on Image Processing*, vol. 7, no. 9, pp. 1300 - 1310, Institute of Electrical and Electronics Engineers, Dec 1998.
The definitive version is available at https://doi.org/10.1109/83.709662

An Image Model Based on Occluding Object Images and Maximum Entropy

John A. Stuller and Rahul Shah

***Abstract*— This paper introduces a statistical image model based on occlusion and maximum entropy. The statistical model combines a fundamental property of image formation, occlusion, with both object-image shape and nonuniform object-image intensity. The model is a composition of individual object-images that have random positions, shapes, and intensities, and that occlude both background and one another. We derive the autocorrelation and second-order probability density functions of this model and give several examples.**

***Index Terms*—Image autocorrelation, image model, occlusion.**

I. Introduction

THIS paper introduces a statistical image model that relates second-order image statistics to the shapes, textures, and occlusion of the object images comprising the image. Emphasis is placed on the two-dimensional (2-D) autocorrelation function (or equivalently, the autocovariance function), of the image, since, as is well known, this function plays a central role in a large number of image processing and coding applications. It is widely accepted that the autocorrelation function of many images can be approximated by a double-sided exponential. The image model introduced here contributes theoretical understanding to the conditions under which the approximately exponential shape does or does not arise.

We can group statistical image models into two classes: 1) image models that are primarily extensions of classical one-dimensional (1-D) time-series models [7], [19], and 2) image models that account for special properties of images or of image formation. The model introduced in this paper lies in class 2. Like other models of class 2, it relates image features to image statistics. One of the earliest examples of a class-2 image model was proposed by Franks [4]. Franks modeled the intensity edges along an image line by the discontinuities in a piecewise-uniform 1-D process. He derived the autocorrelation function of his model and used it to describe the power spectrum of the video line-scan process. A significant extension of Franks' model to two dimensions was proposed by Modestino *et al.* [11] who modeled intensity edges in an image by the discontinuities in a piecewise-uniform, 2-D random process. They derived the associated autocorrelation function and applied it to image coding, edge detection, enhancement, and texture discrimination. Sera [14] described Boolean image models using a key formula of Matheron [9], [10]. The Boolean image models provided a statistical description of the union of occluding, randomly placed, object-image domains, among other properties. The image model of the present paper extends these previous models by allowing for nonstationary background and nonuniform object-image intensity ("texture") as well as random object shape and occlusion of one object by another.

This paper is organized as follows. Section II contains necessary mathematical preliminaries: we define a "preliminary image model" consisting of background and n occluding object images placed randomly on the finite plane, $[-L, L]^2$ and we derive the (ensemble average) mean and autocovariance functions of this preliminary image model. In Section III, we define the "final image model" as the limit $L \to \infty$ of the preliminary model, where $n = 4\lambda L^2$. Thus, the final image model is defined on the real plane, R^2, and has a density, λ, of object images per unit area. More precisely, λ is the expected number of object image center points per unit area. A comparison between the theoretical predictions and experimental mean and autocovariance functions is also presented in Section III. Section IV concludes the development with related results for image line scans. Certain analytical derivations are relegated to Appendixes A and B. A development of the bivariate probability density function (pdf) associated with the model is given in Appendix C.

II. The Preliminary Model: n Object Images on $[-L, L]^2$

The preliminary model consists of n object images placed at random on the finite plane $[-L, L]^2$. Specifically, the preliminary image model, $s_n(\mathbf{x})$, $\mathbf{x} = (x, y) \in [-L, L]^2$, is defined as a 2-D stochastic process composed of a nonstationary stochastic *background image*, $b(\mathbf{x})$, and n randomly placed stochastic *object images*, $o_i(\mathbf{x} - \mathbf{p}_i)$, $i = 1, 2, \cdots, n$. $\mathbf{p}_i = (p_{xi}, p_{yi})$ is the random position vector for the ith object image. The object images are assumed to have the form

$$o_i(\mathbf{x}) = I_i(\mathbf{x}) I(\mathbf{x}; \mathbf{v}_i) \tag{1}$$

where "intensity," $I_i(\mathbf{x})$, is a sample function of a wide-sense stationary process, and

$$I(\mathbf{x}; \mathbf{v}_i) = \begin{cases} 1, & \text{for } \mathbf{x} \in \mathcal{DO}(\mathbf{v}_i) \\ 0, & \text{otherwise} \end{cases} \tag{2}$$

Manuscript received September 23, 1995; revised November 5, 1997. This work was supported by the National Science Foundation under Grant MIP-9223020. The associate editor coordinating the review of this manuscript and approving it for publication was Prof. C.-C. Jay Kuo.

J. A. Stuller is with the Department of Electrical and Computer Engineering, University of Missouri-Rolla, Rolla, MO 65409-0040 USA (e-mail: stuller@ece.umr.edu).

R. Shah is with Qualcomm, Inc., San Diego, CA 92121 USA (e-mail: rshah@qualcomm.com).

Publisher Item Identifier S 1057-7149(98)06394-5.

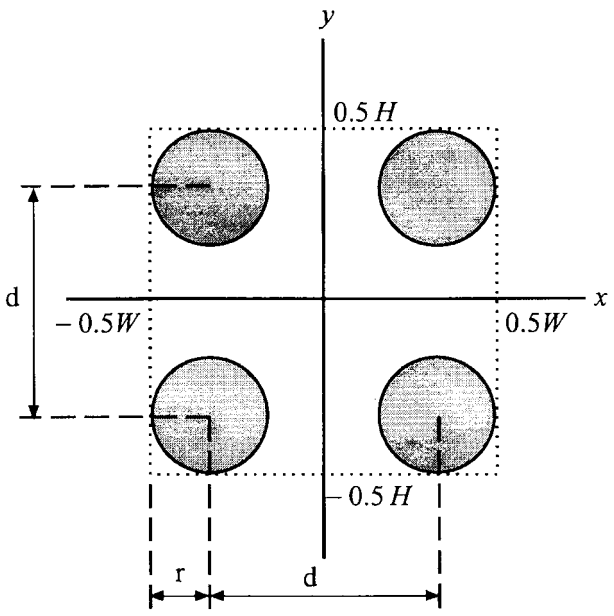

Fig. 1. A possible $\mathcal{DO}(v)$ and bounding rectangle. The interior of the four shaded disks is $\mathcal{DO}(v)$: $v = (r, d), W(v) = H(v) = 2r + d$.

indicates the region of support, $\mathcal{DO}(\mathbf{v}_i)$, of $o_i(\mathbf{x})$. The region of support is defined by a random *shape vector*, $\mathbf{v}_i = (v_{i1}, v_{i2}, \cdots, v_{iM})$, and is centered so that the bounding rectangle $[-W_i/2, W_i/2] \times [-H_i/2, H_i/2]$ touches the boundary of $\mathcal{DO}(\mathbf{v}_i)$ on all four sides as illustrated in Fig. 1. As illustrated in the figure, $\mathcal{DO}(\mathbf{v}_i)$ need not be connected. Clearly, the dimensions of the bounding rectangle depend on $\mathbf{v}_i : W_i = W(\mathbf{v}_i)$ and $H_i = H(\mathbf{v}_i)$.

The principle of *maximum entropy* [6] enables us to obtain the autocovariance function and bivariate pdf of this preliminary image model while being maximally noncommittal with respect to assumptions of intensity and positions. For maximum entropy, object image intensities, shape vectors, and positions will be *mutually independent*. Also, $\mathbf{p}_i$ will be *uniformly distributed* over a domain just large enough so that at least a part of $o_i(\mathbf{x} - \mathbf{p}_i)$ appears in $[-L, L]^2$. Thus, the conditional pdf of $\mathbf{p}_i$ given $\mathbf{v}_i = \mathbf{V}$ is

$$f^{(L)}_{\mathbf{p}_i|\mathbf{v}_i}(\mathbf{P} \mid \mathbf{V}) = \begin{cases} \left(\frac{1}{2L+W(\mathbf{V})}\right)\left(\frac{1}{2L+H(\mathbf{V})}\right), & \text{for } \mathbf{P} \in \mathcal{DI}^+(\mathbf{V}) \\ 0, & \text{otherwise} \end{cases} \tag{3}$$

where $\mathcal{DI}^+(\mathbf{V}) = [-L - 0.5H(\mathbf{V}),\ L + 0.5H(\mathbf{V})] \times [-L - 0.5W(\mathbf{V}), L + 0.5W(\mathbf{V})]$. We assume that the shape vectors are identically distributed and have pdf $p_{\mathbf{v}}(\mathbf{V})$ in the limit $L \to \infty$. For arbitrary L, we define the pdf of $\mathbf{v}$ as

$$\begin{aligned} f^{(L)}_{\mathbf{v}}(\mathbf{V}) &= p_{\mathbf{v}}(\mathbf{V} \mid \mathcal{DO}(\mathbf{v}) \subset [-L, L]^2) \\ &= \begin{cases} \frac{p_{\mathbf{v}}(\mathbf{V})}{\int_{\sigma \in \Psi(L)} p_{\mathbf{v}}(\sigma)\, d\sigma}, & \mathbf{V} \in \Psi(L) \\ 0, & \mathbf{V} \notin \Psi(L) \end{cases} \end{aligned} \tag{4}$$

where $\Psi(L) = \{\mathbf{V} : \mathcal{DO}(\mathbf{V}) \subset [-L, L]^2\}$. It follows from (4) that

$$\lim_{L \to \infty} f^{(L)}_{\mathbf{v}}(\mathbf{V}) = p_{\mathbf{v}}(\mathbf{V}). \tag{5}$$

Since images are created by a perspective transformation of the three-dimensional (3-D) world onto the image plane, images of objects in the foreground occlude images of objects in the background. To account for occlusion, we generate the image recursively. At the ith step of the recursion, $i = 1, 2, \cdots, n$,

$$s_i(\mathbf{x}) = \begin{cases} o_i(\mathbf{x} - \mathbf{p}_i), & \text{if } \mathbf{x} \in \mathcal{DO}_i + \mathbf{p}_i \\ s_{i-1}(\mathbf{x}), & \text{otherwise} \end{cases} \tag{6}$$

where $s_0(\mathbf{x}) \equiv b(\mathbf{x})$ and $\mathbf{x} \in [-L, L]^2$. Thus, at recursion step i, object image $o_i(\mathbf{x} - \mathbf{p}_i)$, is superimposed on the $s_{i-1}(\mathbf{x})$ in such a way such that it occludes $s_{i-1}(\mathbf{x})$ for $\mathbf{x} \in \mathcal{DO}_i + \mathbf{p}_i$. Equation (6) can be written as

$$s_i(\mathbf{x}) = o_i(\mathbf{x} - \mathbf{p}_i) + s_{i-1}(\mathbf{x}) I^c(\mathbf{x} - \mathbf{p}_i; \mathbf{v}_i) \tag{7}$$

where

$$I^c(\mathbf{x}; \mathbf{v}_i) = 1 - I(\mathbf{x}; \mathbf{v}_i). \tag{8}$$

Define $\underline{\mathbf{v}}_i = (\mathbf{v}_1, \mathbf{v}_2, \cdots, \mathbf{v}_i)$ and $\underline{\mathbf{p}}_i = (\mathbf{p}_1, \mathbf{p}_2, \cdots, \mathbf{p}_i)$. The following recursion for the conditional mean of $s_i(\mathbf{x})$, given $\underline{\mathbf{v}}_i = \underline{\mathbf{V}}_i$ and $\underline{\mathbf{p}}_i = \underline{\mathbf{P}}_i$, can be obtained directly from (7):

$$\begin{aligned} \eta_{s_i}(\mathbf{x} \mid \underline{\mathbf{V}}_i, \underline{\mathbf{P}}_i) &= \eta_o(\mathbf{x} - \mathbf{P}_i \mid \mathbf{V}_i) \\ &\quad + \eta_{s_{i-1}}(\mathbf{x} \mid \underline{\mathbf{V}}_{i-1}, \underline{\mathbf{P}}_{i-1}) I^c(\mathbf{x} - \mathbf{P}_i; \mathbf{V}_i) \end{aligned} \tag{9}$$

where $\eta_{s_0}(\mathbf{x} \mid \mathbf{V}_0, \mathbf{P}_0) \equiv \eta_{s_0}(\mathbf{x}) \equiv \eta_b(\mathbf{x})$, $\mathbf{x} \in [-L, L]^2$, and $i = 1, 2, \cdots, n$. The conditions in (9) are removed by multiplying both sides by

$$f^{(L)}_{\underline{\mathbf{P}}_i, \underline{\mathbf{V}}_i}(\underline{\mathbf{P}}_i, \underline{\mathbf{V}}_i) = f^{(L)}_{\underline{\mathbf{P}}_i | \underline{\mathbf{V}}_i}(\underline{\mathbf{P}}_i \mid \underline{\mathbf{V}}_i) f^{(L)}_{\underline{\mathbf{V}}_i}(\underline{\mathbf{V}}_i) \tag{10}$$

and integrating over all $\underline{\mathbf{P}}_i, \underline{\mathbf{V}}_i$. This yields (see Appendix A)

$$\eta_{s_i}(\mathbf{x}) = \eta_I(1 - \xi) + \eta_{s_{i-1}}(\mathbf{x})\xi \tag{11}$$

for $\mathbf{x} \in [-L, L]^2$, $i = 1, 2, \cdots, n$, where $\eta_I = E\{I(\mathbf{x})\}$is constant, and ξ is defined by A1. The solution to (11) is

$$\eta_{s_n}(\mathbf{x}) = \eta_I(1 - \xi^n) + \eta_b(\mathbf{x})\xi^n. \tag{12}$$

The derivation of image autocovariance can be substantially shortened if we temporarily assume that $\eta_I = \eta_b(\mathbf{x}) = 0$. We use a prime on s of (7) to emphasize this assumption. The following recursion for the conditional autocovariance (or autocorrelation) function of $s'_i(\mathbf{x})$ is obtained directly from (7):

$$\begin{aligned} &K_{s'_i}(\mathbf{x}_1, \mathbf{x}_2 \mid \underline{\mathbf{V}}_i, \underline{\mathbf{P}}_i) \\ &\quad = K_o(\mathbf{x}_1 - \mathbf{P}_i, \mathbf{x}_2 - \mathbf{P}_i \mid \mathbf{V}_i) \\ &\qquad + K_{s'_{i-1}}(\mathbf{x}_1, \mathbf{x}_2 \mid \underline{\mathbf{V}}_{i-1}, \underline{\mathbf{P}}_{i-1}) \\ &\qquad \times I^c(\mathbf{x}_1 - \mathbf{P}_i; \mathbf{V}_i) I^c(\mathbf{x}_2 - \mathbf{P}_i; \mathbf{V}_i) \end{aligned} \tag{13}$$

with $K_{s'_0}(\mathbf{x}_1, \mathbf{x}_2 \mid \underline{\mathbf{V}}_0, \underline{\mathbf{P}}_0) \equiv K_{s'_0}(\mathbf{x}_1, \mathbf{x}_2) \equiv K_b(\mathbf{x}_1, \mathbf{x}_2)$, $\mathbf{x}_1, \mathbf{x}_2 \in [-L, L]^2$, $i = 1, 2, \cdots, n$, and

$$\begin{aligned} &K_o(\mathbf{x}_1 - \mathbf{P}_i, \mathbf{x}_2 - \mathbf{P}_i \mid \mathbf{V}_i) \\ &\quad = K_I(\boldsymbol{\Delta}) I(\mathbf{x}_1 - \mathbf{P}_i; \mathbf{V}_i) I(\mathbf{x}_2 - \mathbf{P}_i; \mathbf{V}_i) \end{aligned} \tag{14}$$

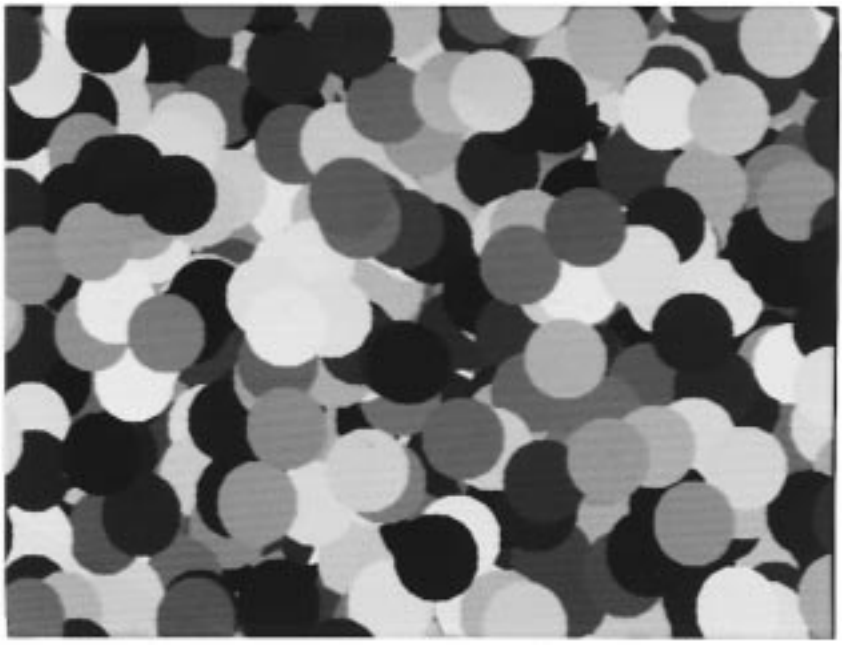

Fig. 2. Image of Example 1.

where $\boldsymbol{\Delta} = \mathbf{x}_2 - \mathbf{x}_1$. We remove the conditions from (13) in a manner similar to (9). The result is

$$K_{s_i'}(\mathbf{x}, \mathbf{x}+\boldsymbol{\Delta}) = K_I(\boldsymbol{\Delta})[\phi(\boldsymbol{\Delta}) - \theta(\boldsymbol{\Delta})] + K_{s_{i-1}'}(\mathbf{x}, \mathbf{x}+\boldsymbol{\Delta})\phi(\boldsymbol{\Delta}) \tag{15}$$

for $\mathbf{x}, \mathbf{x}+\boldsymbol{\Delta} \in [-L, L]^2$ and $i = 1, 2, \cdots, n$ where $\phi(\boldsymbol{\Delta})$ and $\theta(\boldsymbol{\Delta})$are defined by (B1) and (B2). The solution to (15) is

$$K_{s_n'}(\mathbf{x}, \mathbf{x}+\boldsymbol{\Delta}) = K_I(\boldsymbol{\Delta})\frac{\phi(\boldsymbol{\Delta}) - \theta(\boldsymbol{\Delta})}{1-\phi(\boldsymbol{\Delta})}[1 - \phi^n(\boldsymbol{\Delta})] + K_b(\mathbf{x}, \mathbf{x}+\boldsymbol{\Delta})\phi^n(\boldsymbol{\Delta}). \tag{16}$$

III. The Final Image Model: λ Object Images Per Unit Area on R^2

As stated in the Introduction, we define the "final image model" as the limit $L \to \infty$ of the preliminary model, where $n = 4\lambda L^2$. Expressions for the mean, (12), and autocovariance functions (16), become analytically simpler in this limit. The work required to obtain the limit is relegated to the appendices. The limiting form of the mean, $\eta_{s_n}(\mathbf{x})$, (12), is (see Appendix A)

$$\eta_s(\mathbf{x}) = \eta_I(1 - e^{-\lambda\bar{A}}) + \eta_b(\mathbf{x})e^{-\lambda\bar{A}} \tag{17}$$

for $\mathbf{x} \in \mathcal{R}^2$ where $\bar{A}$ is the mean object-image area:

$$\bar{A} \triangleq \int_{-\infty}^{\infty} A(\mathbf{V})p_{\mathbf{v}}(\mathbf{V})\,d\mathbf{V} \tag{18}$$

and $A(\mathbf{V})$ is the object domain area when $\mathbf{v} = \mathbf{V}$

$$A(\mathbf{V}) = \int_{-\infty}^{\infty} I(\mathbf{x}; \mathbf{V})\,d\mathbf{x} = \int_{\mathcal{DO}(\mathbf{V})} d\mathbf{x}. \tag{19}$$

Similarly, the limiting form of the autocovariance, (16), is (see Appendix B)

$$K_{s'}(\mathbf{x}, \mathbf{x}+\boldsymbol{\Delta}) = K_I(\boldsymbol{\Delta})\left\{\frac{\bar{\mathcal{C}}_n(\boldsymbol{\Delta})}{2 - \bar{\mathcal{C}}_n(\boldsymbol{\Delta})}\right\}\{1 - e^{-\lambda\bar{A}[2-\bar{\mathcal{C}}_n(\boldsymbol{\Delta})]}\} + K_b(\mathbf{x}, \mathbf{x}+\boldsymbol{\Delta})e^{-\lambda\bar{A}[2-\bar{\mathcal{C}}_n(\boldsymbol{\Delta})]} \tag{20}$$

for $\mathbf{x} \in \mathcal{R}^2$, where $\bar{\mathcal{C}}_n(\boldsymbol{\Delta})$ is the normalized expected value of the *object-domain spatial correlation function*

$$\mathcal{C}(\boldsymbol{\Delta}; \mathbf{V}) \triangleq \int_{-\infty}^{\infty} I(\mathbf{x}; \mathbf{V})I(\mathbf{x}+\boldsymbol{\Delta}; \mathbf{V})\,d\mathbf{x}. \tag{21}$$

That is, with

$$\bar{\mathcal{C}}(\boldsymbol{\Delta}) = E\{\mathcal{C}(\boldsymbol{\Delta}; \mathbf{V})\} = \int_{-\infty}^{\infty} \mathcal{C}(\boldsymbol{\Delta}; \mathbf{V})p_{\mathbf{v}}(\mathbf{V})\,d\mathbf{V} \tag{22}$$

we have

$$\bar{\mathcal{C}}_n(\boldsymbol{\Delta}) = \bar{\mathcal{C}}(\boldsymbol{\Delta})/\bar{\mathcal{C}}(\mathbf{0}) = \bar{\mathcal{C}}(\boldsymbol{\Delta})/\bar{\mathcal{A}}. \tag{23}$$

We can use (17) to find $P_b(0) \equiv \Pr\{B(\mathbf{x})\}$ where $B(\mathbf{x}) = \{$background appears (is not occluded) at $\mathbf{x}\}$, and $P_o(0) \equiv \Pr\{O(\mathbf{x})\} = 1 - P_b(0)$ where $O(\mathbf{x}) = \{$an object-image appears at $\mathbf{x}\}$. By comparing (17) with

$$\eta_s(\mathbf{x}) = \eta_b(\mathbf{x})P_b(0) + \eta_I P_o(0) \tag{24}$$

we obtain

$$P_b(0) = e^{-\lambda\bar{A}} \tag{25}$$

$$P_o(0) = 1 - e^{-\lambda\bar{A}}. \tag{26}$$

Similarly, we can use (20) to find $P_b(\boldsymbol{\Delta}) = \Pr\{B(\mathbf{x})B(\mathbf{x}+\boldsymbol{\Delta})\}$ and $P_o(\boldsymbol{\Delta}) = \Pr\{O(\mathbf{x}, \mathbf{x}+\boldsymbol{\Delta})\}$ where $B(\mathbf{x})B(\mathbf{x}+\boldsymbol{\Delta})$ is the event $\{$background appears at both $\mathbf{x}$ and $\mathbf{x}+\boldsymbol{\Delta}\}$ and $O(\mathbf{x}, \mathbf{x}+\boldsymbol{\Delta})$ is the event $\{$parts of the *same* object are visible at $\mathbf{x}$ and $\mathbf{x}+\boldsymbol{\Delta}\}$.

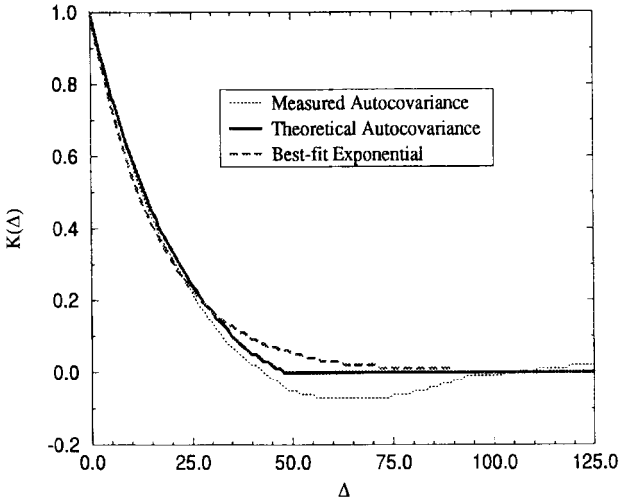

Fig. 3. Autocovariance functions of Example 1.

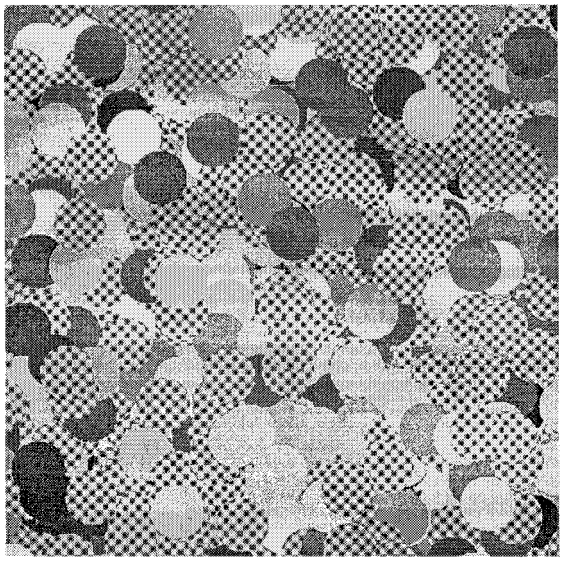

Fig. 4. Image of Example 2.

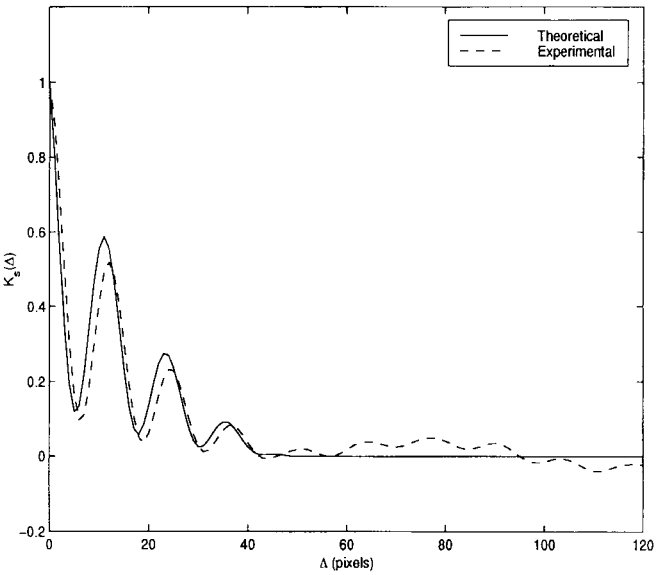

Fig. 5. Autocovariance functions of Example 2.

(We use product notation for set intersection, i.e., for any two sets, X and Y, $XY \equiv X \cap Y$.) By comparing (20) with the identity

$$K_{s'}(\mathbf{x},\mathbf{x}+\boldsymbol{\Delta}) = K_I(\boldsymbol{\Delta})P_o(\boldsymbol{\Delta}) + K_b(\mathbf{x},\mathbf{x}+\boldsymbol{\Delta})P_b(\boldsymbol{\Delta}) \quad (27)$$

we obtain

$$P_b(\boldsymbol{\Delta}) = e^{-\lambda\bar{A}[2-\bar{C}_n(\boldsymbol{\Delta})]} \quad (28)$$

$$P_o(\boldsymbol{\Delta}) = \left\{\frac{\bar{C}_n(\boldsymbol{\Delta})}{2-\bar{C}_n(\boldsymbol{\Delta})}\right\}\{1 - e^{-\lambda\bar{A}[2-\bar{C}_n(\boldsymbol{\Delta})]}\}. \quad (29)$$

Notice that $P_b(\boldsymbol{\Delta})$ decreases exponentially with λ while $P_o(\boldsymbol{\Delta})$ increases with λ. This behavior reflects the increasing object-image density for increasing λ. Additional probabilities of interest are readily obtained. For example, the probability that background appears at a point $\mathbf{x}_2 = \mathbf{x} + \boldsymbol{\Delta}$ given that background appears at a point $\mathbf{x}_1 = \mathbf{x}$ is

$$\Pr\{B(\mathbf{x}_2) \mid B(\mathbf{x}_1)\} = \frac{\Pr\{B(\mathbf{x}_1)B(\mathbf{x}_2)\}}{\Pr\{B(\mathbf{x}_1)\}} = \frac{P_b(\boldsymbol{\Delta})}{P_b(0)} = \frac{e^{-\lambda\bar{A}[2-\bar{C}_n(\boldsymbol{\Delta})]}}{e^{-\lambda\bar{A}}} = e^{-\lambda\bar{A}[1-\bar{C}_n(\boldsymbol{\Delta})]}. \quad (30)$$

Similarly

$$\Pr\{O(\mathbf{x}_2) \mid B(\mathbf{x}_1)\} = 1 - e^{-\lambda\bar{A}[1-\bar{C}_n(\boldsymbol{\Delta})]} \quad (31)$$

$$\Pr\{B(\mathbf{x}_1) \mid O(\mathbf{x}_2)\} = \frac{1 - e^{-\lambda\bar{A}[1-\bar{C}_n(\boldsymbol{\Delta})]}}{1 - e^{-\lambda\bar{A}}} e^{-\lambda\bar{A}} \quad (32)$$

$$\Pr\{O(\mathbf{x}_1) \mid O(\mathbf{x}_2)\} = \frac{1 - 2e^{-\lambda\bar{A}} + e^{-\lambda\bar{A}[2-\bar{C}_n(\boldsymbol{\Delta})]}}{1 - e^{-\lambda\bar{A}}} \quad (33)$$

$$\Pr\{O(\mathbf{x}_1)O(\mathbf{x}_2)\} = 1 - 2e^{-\lambda\bar{A}} + e^{-\lambda\bar{A}[2-\bar{C}_n(\boldsymbol{\Delta})]} \quad (34)$$

$$\Pr\{O(\mathbf{x}_2)B(\mathbf{x}_1)\} = (1 - e^{-\lambda\bar{A}[1-\bar{C}_n(\Delta)]})e^{-\lambda\bar{A}}. \quad (35)$$

Equation (34) gives the probability of the event $O(\mathbf{x}_1)O(\mathbf{x}_2) = \{$*an* object is visible at $\mathbf{x}_1$ AND *an* object is visible at $\mathbf{x}_2\}$ while (29) gives the probability of the event $O(\mathbf{x},\mathbf{x}+\boldsymbol{\Delta}) = \{$parts of the *same* object are visible at $\mathbf{x}$ and $\mathbf{x}+\boldsymbol{\Delta}\}$.

We can extend the autocovariance result (20) to nonzero η_I and $\eta_b(\mathbf{x})$, by writing each sample function $s(\mathbf{x},\zeta)$ of the process $s(\mathbf{x})$ as a sum $s(\mathbf{x},\zeta) = s'(\mathbf{x},\zeta) + s''(\mathbf{x},\zeta)$ where $s''(\mathbf{x},\zeta) = \eta_I$ if an object-image exists at $\mathbf{x}$ and $s''(\mathbf{x},\zeta) = \eta_b(\mathbf{x})$ otherwise. This sum leads directly to the following expression for the autocorrelation function of $s(\mathbf{x})$:

$$\begin{aligned} R_s(\mathbf{x}_1,\mathbf{x}_2) = {} & \left[K_I(\mathbf{x}_2-\mathbf{x}_1) + \eta_I^2\right]\Pr\{O(\mathbf{x}_1)O(\mathbf{x}_2)\} \\ & + \eta_I\eta_b(\mathbf{x}_2)\Pr\{O(\mathbf{x}_1)B(\mathbf{x}_2)\} \\ & + \eta_b(\mathbf{x}_1)\eta_I\Pr\{B(\mathbf{x}_1)O(\mathbf{x}_2)\} \\ & + R_b(\mathbf{x}_1,\mathbf{x}_2)\Pr\{B(\mathbf{x}_1)B(\mathbf{x}_2)\}. \end{aligned} \quad (36)$$

We also have

$$R_s(\mathbf{x},\mathbf{x}+\boldsymbol{\Delta}) = K_s(\mathbf{x},\mathbf{x}+\boldsymbol{\Delta}) + \eta_s(\mathbf{x})\eta_s(\mathbf{x}+\boldsymbol{\Delta}) \quad (37)$$

where $\eta_s(\mathbf{x})$ is given by (24). When we substitute (34), (35), and $P_b(\boldsymbol{\Delta}) = \Pr\{B(\mathbf{x})B(\mathbf{x}+\boldsymbol{\Delta})\}$ of (28) into (36) and equate

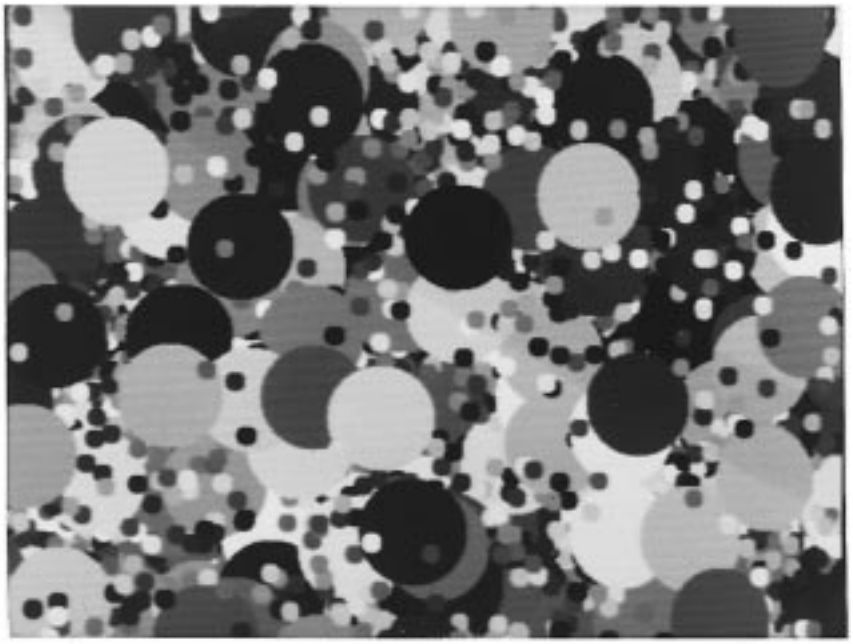

Fig. 6. Image of Example 3.

the result to (37) we obtain

$$K_s(\mathbf{x},\mathbf{x}+\boldsymbol{\Delta}) = K_I(\boldsymbol{\Delta})P_o(\boldsymbol{\Delta}) + K_b(\mathbf{x},\mathbf{x}+\boldsymbol{\Delta})P_b(\boldsymbol{\Delta}) + [\eta_I - \eta_b(\mathbf{x})][\eta_I - \eta_b(\mathbf{x}+\boldsymbol{\Delta})] \times [P_b(\boldsymbol{\Delta}) - P_b(0)^2]. \quad (38)$$

We illustrate the preceding result with five examples in which the experimental images are 512×512 pixels^2 with 8 b/pixel. (Size 390×512 submatrices of the 512×512 image arrays are shown in Figs. 2, 6, 8, and 11.) We define the spacing between pixels to be unity, so $L = 256$. In the examples we compare the experimental (spatial average) and theoretical (ensemble average) autocovariance functions. "Best-fit exponential" approximations [15] to the experimental autocovariance functions are also presented for comparison. The autocovariance functions have been normalized in the plots. All 1-D autocovariance function plots are for $\boldsymbol{\Delta} = (\Delta, 0)$. In examples 1, 2, 3, and 5, the object-image density is high, i.e., $\lambda\bar{A} \gg 1 \Rightarrow P_b(0) \approx 0$, for which (38) is well approximated by

$$K_s(\mathbf{x},\mathbf{x}+\boldsymbol{\Delta}) \approx K_I(\boldsymbol{\Delta})P_o(\boldsymbol{\Delta}) \approx K_I(\boldsymbol{\Delta})\left\{\frac{\bar{\mathcal{C}}_n(\boldsymbol{\Delta})}{2-\bar{\mathcal{C}}_n(\boldsymbol{\Delta})}\right\}. \quad (39)$$

Example 1: Each object image is a disk having known radius $r = 25$. Thus, $\bar{A} = \pi(25)^2$. The intensity, $I(\mathbf{x})$, is a constant, I, that varies at random in the range $[0, 255]$ from disk to disk. There are $\lambda = 0.038$ disks per unit area, so $\lambda\bar{A} \approx 75 \gg 1$. A sample image is shown in Fig. 2.

Since $I(\mathbf{x})$ is a random constant, then $K_I(\boldsymbol{\Delta}) = \sigma_I^2$ where σ_I^2 is the variance of I. To obtain $\bar{\mathcal{C}}_n(\boldsymbol{\Delta})$, we set $\mathbf{v}$ to the scalar $v = r$, so $\mathcal{DO}(v) = \{\mathbf{x} : |\mathbf{x}| \le v\}$ and

$$I(\mathbf{x};r) = \begin{cases} 1, & \text{for } |\mathbf{x}| \le r \\ 0, & \text{otherwise} \end{cases}$$

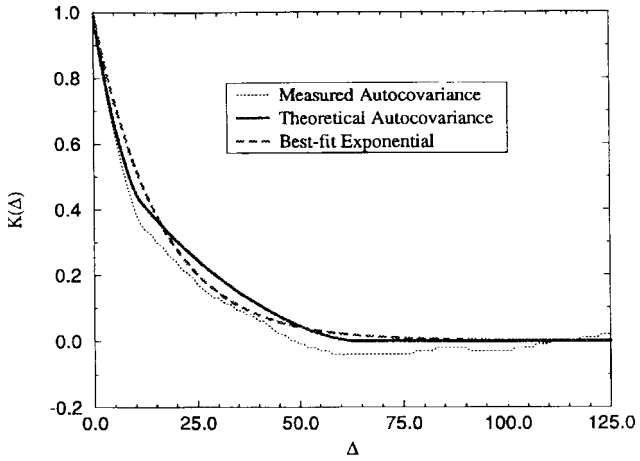

Fig. 7. Autocovariance functions of Example 3.

with $p_{\mathbf{v}}(\mathbf{V}) = \delta(V - r)$. Straightforward evaluation of (21)–(23) yields

$$\bar{\mathcal{C}}_n(\boldsymbol{\Delta}) = \left(\frac{2}{\pi}\cos^{-1}\frac{|\boldsymbol{\Delta}|}{2r} - \frac{|\boldsymbol{\Delta}|}{\pi r}\sqrt{1-\frac{|\boldsymbol{\Delta}|^2}{4r^2}}\right) I(\boldsymbol{\Delta};2r). \quad (40)$$

The autocovariance function is given by (39). The expression for $P_o(\boldsymbol{\Delta})$ of (29) is related to a formula of Matheron [9], [10] for Boolean-image disks as described in [14]. The experimental, theoretical and best-fit exponential autocovariance functions are shown in Fig. 3. The discrepancy between the theoretical prediction and the experimental result for $|\boldsymbol{\Delta}| \approx 2r = 50$ is due to the finite size of the sample image. As expected, measurements on sample images larger than that of Fig. 2 yield closer agreement between theory and experiment [17].

Example 2: Each object image is a disk having known radius r as in Example 1. However, the intensity $I(\mathbf{x})$ is

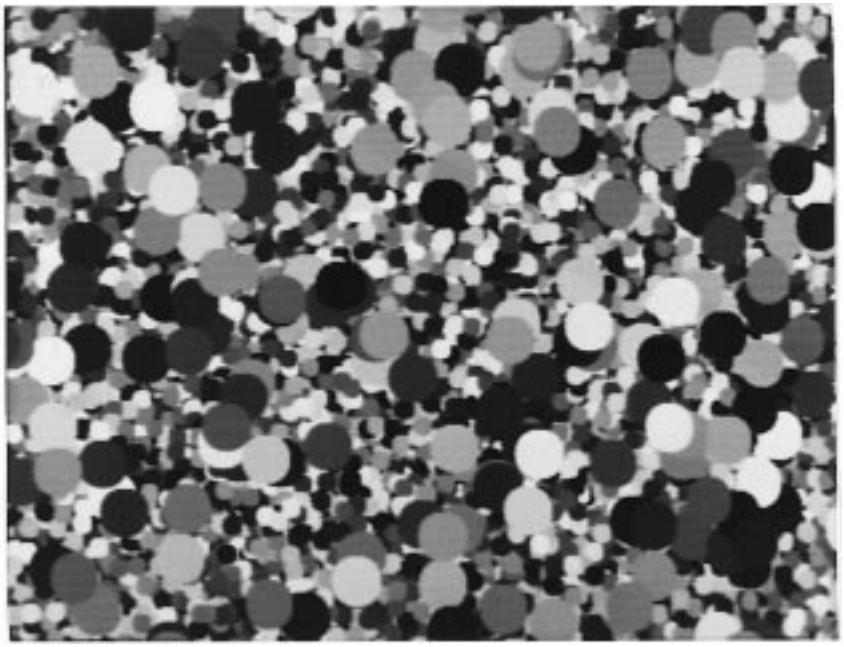

Fig. 8. Image of Example 4.

selected at random from one of the following two ensembles: 1) $I(\mathbf{x}) = I$ where I is a random variable as in Example 1, or 2) $I(\mathbf{x}) = a + b\cos(\omega x + \phi_1)\cos(\omega y + \phi_2)$ where a, b, and $\omega = 2\pi f$ are known constants and (ϕ_1, ϕ_2) is a point selected at random on $[0, 2\pi]^2$. Disks having intensities selected from ensemble 1 will be similar to those of Example 1. Disks having intensities selected from ensemble 2 will have 2-D sinusoidal intensities with phases differing at random from disk to disk. A sample image is shown in Fig. 4 for $a = b = 128, r = 12.5$ and $f = 6.25$ (four intensity cycles across a disk). A standard analysis reveals that

$$K_I(\boldsymbol{\Delta}) = \frac{\sigma_I^2}{4} + \frac{b^2}{16}\cos(\omega\Delta_x)\cos(\omega\Delta_y).$$

$\bar{C}_n(\boldsymbol{\Delta})$ is identical to that of Example 1. Again, the autocovariance function is given by (39). The experimental and theoretical autocovariance functions are shown in Fig. 5.

Example 3: The image ensemble is composed of object images that are disks of random radii $r_1 = 6$ and $r_2 = 32$ having probabilities $P_1 = 0.91$ and $P_2 = 0.09$, and densities $\lambda_1 = 0.038$ and $\lambda_2 = 0.0038$, respectively. Object-image intensity, $I(\mathbf{x})$, is as in Example 1. Fig. 6 shows a sample from this image ensemble.

The mean object area is $\bar{A} = 0.91 \times \pi 6^2 + 0.09 \times \pi(32)^2 \approx 395$ and the density is $\lambda = \lambda_1 + \lambda_2 \approx 0.042$. Thus, $\lambda\bar{A} \approx 16 \gg 1$. The normalized mean object-indicator function is

$$\bar{C}_n(\boldsymbol{\Delta}) = \frac{1}{\bar{A}}\sum_{i=1}^{2} P_i\left(\frac{2}{\pi}\cos^{-1}\frac{|\boldsymbol{\Delta}|}{2r_i} - \frac{|\boldsymbol{\Delta}|}{\pi r_i}\sqrt{1 - \frac{|\boldsymbol{\Delta}|^2}{4r_i^2}}\right) I(\boldsymbol{\Delta}; 2r_i)$$

where $I(\cdot)$ is defined in Example 1. Fig. 7 shows the theoretical, the least-squares exponential approximation to the theoretical, and the measured autocovariances of this image.

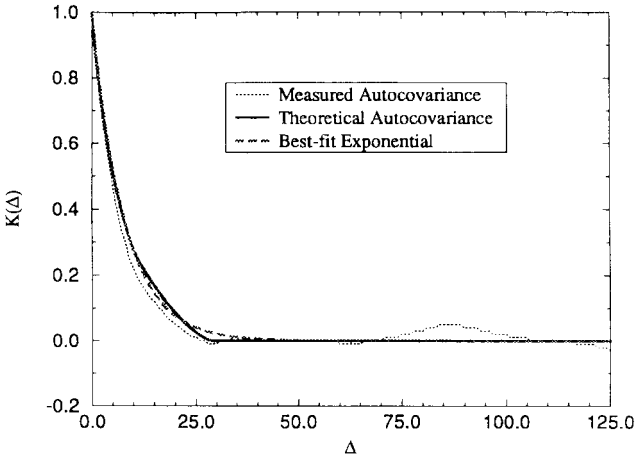

Fig. 9. Autocovariance functions of Example 4.

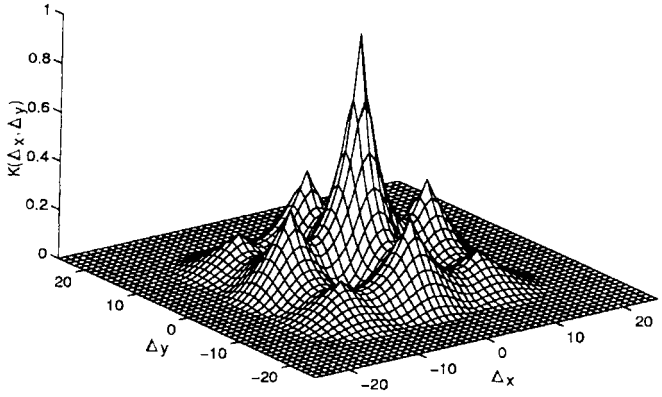

Fig. 10. Two-dimensional autocovariance functions of Example 5.

Notice that the measured autocovariance curve appears to have a discontinuous slope at shift $|\boldsymbol{\Delta}| = 2r_1 = 12$ in agreement with the theoretical prediction.

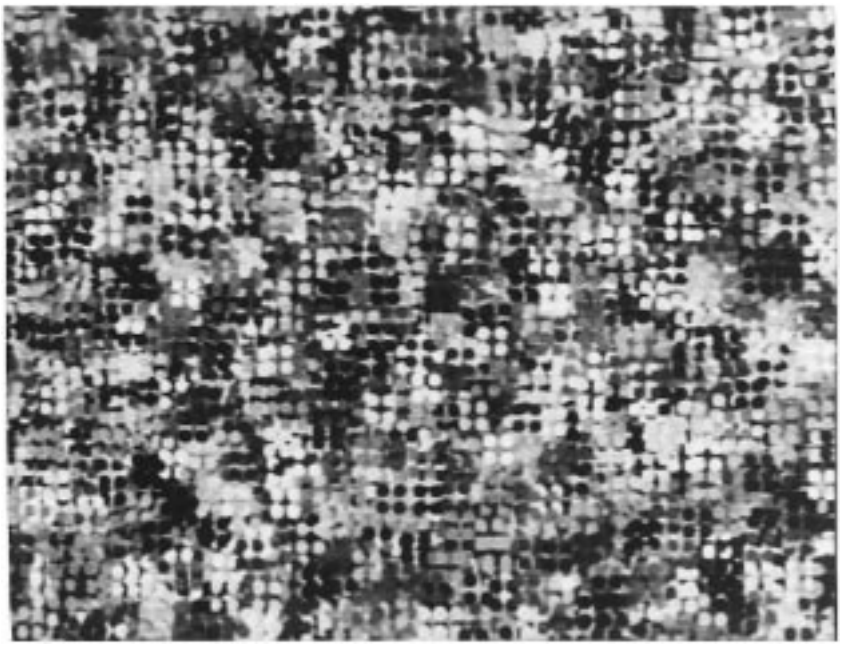

Fig. 11. Image of Example 5.

Example 4: This image ensemble is composed of visible background, $b(\mathbf{x})$ as well as object images. The background consists of occluding disks identical to Example 1 but having radius $r_b = 6$. The density of the background disks, λ_b, satisfies $\lambda_b \bar{A}_b \gg 1$ where $\bar{A}_b = \pi r_b^2$. The object images occluding the background are disks of radius $r_o = 15$. The density of the object-images disks, λ_o, was chosen to be 9.478×10^{-4} so $\lambda_o \bar{A}_o = \lambda_o \pi r_o^2 = 0.67 \not\gg 1$ and $P_b(0) \approx 0.5$. A sample image is shown in Fig. 8.

Since $\lambda_b \bar{A}_b \gg 1$, we can use (39) to find the covariance of the background

$$K_b(\mathbf{x}, \mathbf{x}+\boldsymbol{\Delta}) \approx K_I(\boldsymbol{\Delta}) P_b(\boldsymbol{\Delta}) = \sigma_I^2 P_{o_1}(\boldsymbol{\Delta})$$

where $K_I(\boldsymbol{\Delta}) = \sigma_I^2$, and $P_{o_1}(\boldsymbol{\Delta}) = P_o(\boldsymbol{\Delta})|_{r=r_b}$ and $P_o(\boldsymbol{\Delta})$ is given by (29) with $\bar{\mathcal{C}}_n(\boldsymbol{\Delta})$ given by (40). Since $\eta_I = \eta_b(\mathbf{x}) = 128$, (38) yields

$$\begin{aligned} K_s(\mathbf{x}, \mathbf{x}+\boldsymbol{\Delta}) &= K_I(\boldsymbol{\Delta}) P_{o_2}(\boldsymbol{\Delta}) + K_b(\mathbf{x}, \mathbf{x}+\boldsymbol{\Delta}) P_{o_1}(\boldsymbol{\Delta}) \\ &= \sigma_I^2 \left[P_{o_2}(\boldsymbol{\Delta}) + P_{o_1}(\boldsymbol{\Delta}) P_b(\boldsymbol{\Delta}) \right] \end{aligned}$$

where $P_{o_2}(\boldsymbol{\Delta}) = P_o(\boldsymbol{\Delta})|_{r=r_o}$. The theoretical and experimental autocovariance functions are shown in Fig. 9 along with the exponential approximation.

Example 5: Object images are four disks, each having radius $r = 4$, centered at the corners of a square as in Fig. 1. The distance between the centers of the nearest neighbors is $d = 10$ and the intensities of the four disks are the same random constant, I, uniformly random in the range $[0, 255]$. Thus, each set of four disks has the same intensity, I, where I varies from set to set. As in Example 1, $K_I(\boldsymbol{\Delta}) = \sigma_I^2$. The expression for $\bar{\mathcal{C}}_n(\boldsymbol{\Delta})$, which is not isotropic, is given in [15]. A plot of the 2-D theoretical autocovariance is shown in Fig. 10. A sample image from this ensemble is shown in Fig. 11. The experimental, theoretical and best-fit exponential autocovariance functions are shown in Fig. 12.

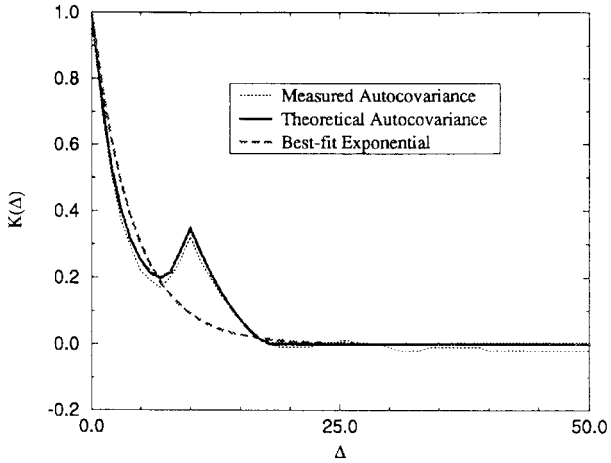

Fig. 12. Autocovariance functions of Example 5.

IV. 1-D (Line-Scan) Image Model

By using analytical steps similar to those in preceding sections, one can obtain the mean and autocovariance functions of a 1-D image model composed of 1-D object-image segments that have random positions and *lengths*, w (before occlusion). Here, 2-D vectors are replaced with scalars: $\mathbf{x} \to x$, $\boldsymbol{\Delta} \to \Delta$. λ becomes the expected number of object-image center points per unit length instead of unit area, and $I(\mathbf{x}; \mathbf{v}_i)$ is replaced with $I(x; w) = 1, x \in [-0.5w, 0.5w]$, $I(x; w) = 0, x \notin [-0.5w, 0.5w]$. The mean object-image area, $\bar{A}$, is replaced by the mean object-image length, $\bar{w}$.

The mean image intensity has the form (24) where

$$P_b(0) \equiv \Pr\{B(x)\} = e^{-\lambda \bar{w}} \tag{41}$$

and $P_o(0) \equiv \Pr\{O(x)\} = 1 - P_b(0)$. Similarly, the 1-D image autocovariance function has the form (38). Here, however, the analysis can go one step further because the object indicator

spatial correlation function, $\mathcal{C}(\mathbf{\Delta};\mathbf{V}) \triangleq \int_{-\infty}^{\infty} I(\mathbf{x};\mathbf{V})I(\mathbf{x}+\mathbf{\Delta};\mathbf{V})\,d\mathbf{x}$, of (21) becomes $\mathcal{C}(\Delta;W) \triangleq \int_{-\infty}^{\infty} I(x;w)I(x+\Delta;w)\,dx$ which is a triangle function with height w and base $2w$ centered at the origin. This triangle function is analogous to the triangle discussed by Schreiber [13]. (In the present paper, however, w represents object-image length before occlusion may occur.) Since an explicit form for $\mathcal{C}(\Delta;W)$ is available, we can also evaluate $\bar{\mathcal{C}}(\Delta;W)$ of (22) explicitly to obtain

$$P_b(\Delta) = e^{-\lambda\bar{w}[1+\psi(\Delta)]} \tag{42}$$

$$P_o(\Delta) = \left\{\frac{1-\psi(\Delta)}{1+\psi(\Delta)}\right\}\{1-e^{-\lambda\bar{w}[1+\psi(\Delta)]}\} \tag{43}$$

where

$$\psi(\Delta) = \frac{1}{\bar{w}}\int_0^{|\Delta|}[1-P_w(W)]\,dW. \tag{44}$$

In (44), $P_w(W)$ is the cumulative distribution function of w: $P_w(W) = \int_0^W p_w(\sigma)\,d\sigma$. $\psi(\Delta)$ is an even-symmetric function of Δ, monotonically increasing in $|\Delta|$ with $\psi(0)=0$ and $\psi(\pm\infty)=1$. Therefore, $P_b(\Delta)$ and $P_o(\Delta)$ are even symmetric functions of Δ, which decrease monotonically with $|\Delta|$ to $P_b(\pm\infty)=\exp(-2\lambda\bar{w})$ and $P_o(\pm\infty)=0$.

Representative plots of $P_o(\Delta)$ are given in Fig. 13. Fig. 13(a) assumes that all object-images have before-occlusion length, W_o, i.e. $p_w(W) = \delta(W-W_o)$. Notice in Fig. 13(a) that $P_o(\Delta)$ is approximately triangular when λ is small. As λ increases, the probability that the same object image is visible for large $|\Delta|$ (i.e. $|\Delta|$ near W_o) decreases relative to that for smaller $|\Delta|$ due to occlusion. Thus, $P_o(\Delta)$ of Fig. 13(a) departs from the triangular shape for large λ. Fig. 13(b) assumes that $p_w(W)$ is exponential: $p_w(W) = (1/\bar{w})\exp\{-W/\bar{w}\}u(W)$ where $u(W)$ is the unit step function. Fig. 13(c) assumes that w is lognormal, i.e. $\ln(w)$ is normal with $E\{\ln(w)\}=\mu$ and $\mathrm{VAR}\{\ln(w)\}=\sigma^2$. A lognormal distribution is of interest because it is claimed to describe the size distributions of various classes of physical objects [1], [3]. Notice from Fig. 13(c) that $P_o(\Delta)$ can have "tails" that extend over large Δ for lognormal w. These tails are related to significant correlation over large distances, Δ, in the autocovariance. The plots in Fig. 13 suggest that $P_o(\Delta)$ has an approximately exponential appearance for a large variety of $p_w(W)$ and λ. However, we can also see from Fig. 13 that $P_o(\Delta)$ is not always well approximated by an exponential.

V. Conclusion

We have introduced an image model that relates second-order intensity statistics to object-image shape, texture, and occlusion and we have presented experiments that support the theoretical predictions of the model. Although the model may prove helpful in predicting the second-order statistics of certain classes of real-life images, we believe that the primary value of this paper may lie in the new insight it provides into the formation of image second-order statistics and in the novel analytical approach for obtaining the model's second-order statistics.

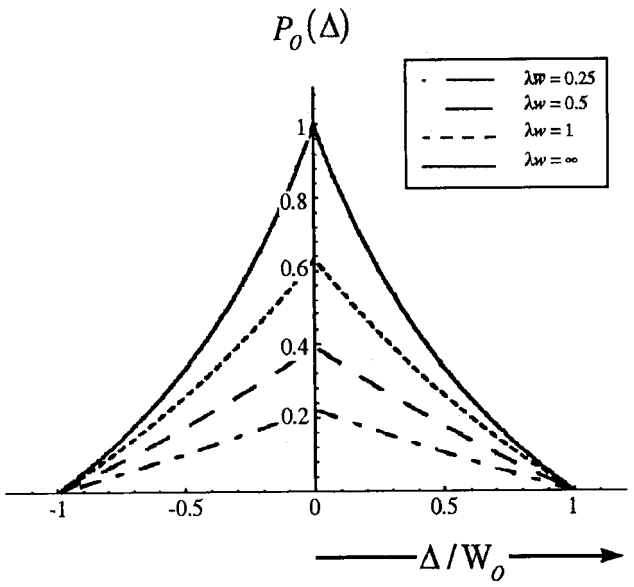

(a)

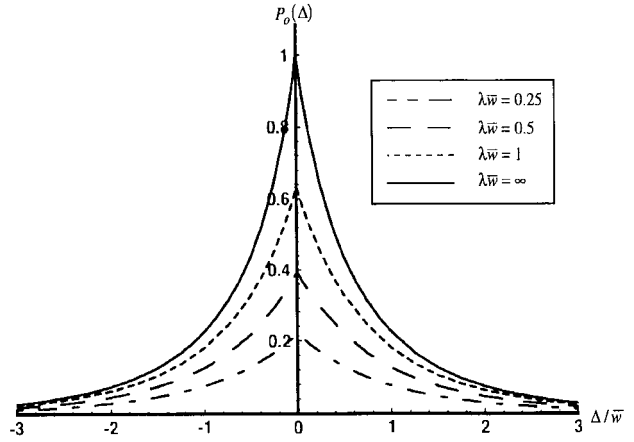

(b)

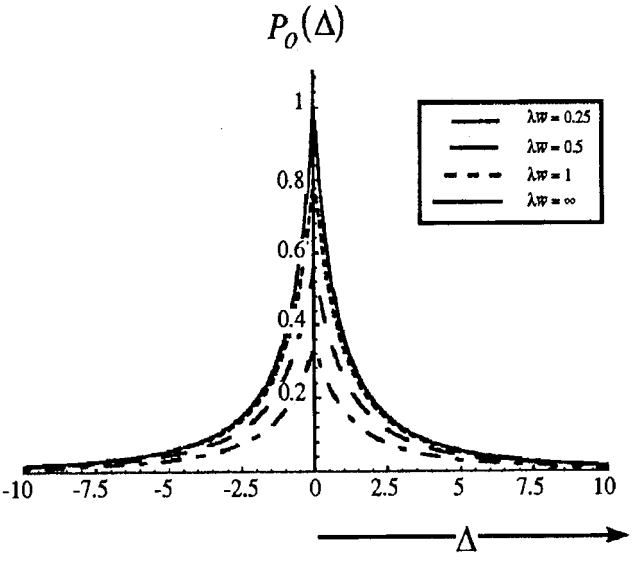

(c)

Fig. 13. $P_o(\Delta)$ versus Δ with parameter λ for various $p_w(W)$. (a) $p_w(W) = \delta(W-W_o)$, (b) $p_w(W) = (1/\bar{w})\exp\{-W/\bar{w}\}u(W)$, (c) w is lognormal: $\ln(w)$ is normal with $E\{\ln(w)\}=0$ and $\mathrm{VAR}\{\ln(w)\}=1$.

APPENDIX A

We show here the steps leading to (11) and (17). As a preliminary development, we evaluate

$$\xi \triangleq E\{I^c(\mathbf{x}-\mathbf{p};\mathbf{v})\} = 1 - E\{I(\mathbf{x}-\mathbf{p};\mathbf{v})\} \tag{A1}$$

for $\mathbf{x} \in [-L, L]^2$. From (3) we find that

$$E\{I(\mathbf{x}-\mathbf{p}_i;\mathbf{v}_i) \mid \mathbf{v}_i = \mathbf{V}_i\} = \frac{1}{[2L+W(\mathbf{V})][2L+H(\mathbf{V})]} A(\mathbf{V})$$

for $\mathbf{x} \in [-L, L]^2$ and $\mathbf{V} \in \Psi(L)$ where $A(\mathbf{V})$ is defined by (19). Removal of the condition $\mathbf{v} = \mathbf{V}$ yields

$$\xi = 1 - \int_{-\infty}^{\infty} \frac{1}{[2L+W(\mathbf{V})][2L+H(\mathbf{V})]} A(\mathbf{V}) f_{\mathbf{v}}^{(L)}(\mathbf{V})\, d\mathbf{V}$$

which, by algebraic manipulations, becomes

$$\xi = 1 - \frac{1}{(2L)^2}\bar{A}(L) + \frac{1}{(2L)^2}\int_{-\infty}^{\infty} A(\mathbf{V}) \times \frac{2L[W(\mathbf{V})+H(\mathbf{V})] + W(\mathbf{V})H(\mathbf{V})}{[2L+H(\mathbf{V})][2L+W(\mathbf{V})]} f_{\mathbf{v}}^{(L)}(\mathbf{V})\, d\mathbf{V} \tag{A2}$$

where

$$\bar{A}(L) = \int_{-\infty}^{\infty} A(\mathbf{V}) f_{\mathbf{v}}^{(L)}(\mathbf{V})\, d\mathbf{V}$$

We now describe the steps leading to (11). When we remove the conditions from the LHS of (9) we obtain the LHS of (11) by definition. Consider the first term on the RHS side of (9):

$$\begin{aligned}\eta_o(\mathbf{x}-\mathbf{P}_i \mid \mathbf{V}_i) &= E\{o(\mathbf{x}-\mathbf{p}_i) \mid \mathbf{p}_i = \mathbf{P}_i, \mathbf{v}_i = \mathbf{V}_i\} \\ &= E\{I(\mathbf{x}-\mathbf{P}_i) I(\mathbf{x}-\mathbf{P}_i;\mathbf{V}_i)\} \\ &= \eta_I\, I(\mathbf{x}-\mathbf{P}_i;\mathbf{V}_i)\end{aligned}$$

Removal of the conditions $\mathbf{p}_i = \mathbf{P}_i, \mathbf{v}_i = \mathbf{V}_i$ yields

$$\eta_I E\{I(\mathbf{x}-\mathbf{p}_i;\mathbf{v}_i)\} = \eta_I(1-\xi)$$

which is the first term on the RHS of (11). Removal of the conditions $\mathbf{p}_i = \mathbf{P}_i, \mathbf{v}_i = \mathbf{V}_i$ for the second term on the RHS of (9) yields

$$\eta_{s_{i-1}}(\mathbf{x}) E\{I^c(\mathbf{x}-\mathbf{p};\mathbf{v})\} = \eta_{s_{i-1}}(\mathbf{x})\xi$$

which is the second term on the RHS of (11).

To derive (17), note that zero is a lower bound for the integral on the RHS of (A2). An upper bound for the same integral is obtained by dropping the $W(\mathbf{V})$ and the $H(\mathbf{V})$ in the denominator and applying the inequality $A(\mathbf{V}) \le W(\mathbf{V})H(\mathbf{V})$. This yields the upper bound

$$\frac{1}{(2L)^3}[m_{21}(L)+m_{12}(L)] + \frac{1}{(2L)^4} m_{22}(L)$$

where

$$m_{21}(L) = \int_{-\infty}^{\infty} W^2(\mathbf{V}) H(\mathbf{V}) f_{\mathbf{v}}^{(L)}(\mathbf{V})\, d\mathbf{V} \tag{A3}$$

$$m_{12}(L) = \int_{-\infty}^{\infty} W(\mathbf{V}) H^2(\mathbf{V}) f_{\mathbf{v}}^{(L)}(\mathbf{V})\, d\mathbf{V} \tag{A4}$$

and

$$m_{22}(L) = \int_{-\infty}^{\infty} W^2(\mathbf{V}) H^2(\mathbf{V}) f_{\mathbf{v}}^{(L)}(\mathbf{V})\, d\mathbf{V}. \tag{A5}$$

It follows from (A2) that

$$1 - \frac{1}{(2L)^2}\bar{A}(L) < \xi < 1 - \frac{1}{(2L)^2}\bar{A}(L) + \frac{1}{(2L)^3}[m_{21}(L)+m_{12}(L)] + \frac{1}{(2L)^4} m_{22}(L).$$

$\bar{A}(L), m_{21}(L), m_{12}(L)$ and $m_{22}(L)$ are all nonnegative. They are also all bounded functions of L because we have assumed that $\mathcal{DO}(\mathbf{V})$ can be drawn physically. If we operate on the above inequality with $\lambda(2L)^2 \log_e$ and use the inequality

$$\epsilon - \epsilon^2 < \ln(1+\epsilon) < \epsilon \tag{A6}$$

for $|\epsilon| < 0.5$, we obtain, for sufficiently large L

$$-\lambda\bar{A}(L) - \lambda\left[\frac{\bar{A}(L)}{2L}\right]^2 < \ln \xi^{\lambda(2L)^2} < -\lambda\bar{A}(L) + \frac{\lambda}{2L}[m_{21}(L)+m_{12}(L)] + \frac{\lambda}{(2L)^2} m_{22}(L).$$

It follows that $\xi^{\lambda(2L)^2} \to e^{-\lambda\bar{A}}$ as $L \to \infty$ where

$$\bar{A} \triangleq \lim_{L\to\infty} \bar{A}(L) = \int_{-\infty}^{\infty} A(\mathbf{V}) p_{\mathbf{v}}(\mathbf{V})\, d\mathbf{V}.$$

Therefore, (12) becomes (17) in the limit $L \to \infty$ with $n = 4\lambda L^2$.

APPENDIX B

We show here the steps leading to (20). As a preliminary step, we evaluate

$$\phi(\mathbf{\Delta}) \triangleq E\{I^c(\mathbf{x}_1-\mathbf{p}_i;\mathbf{v}_i) I^c(\mathbf{x}_2-\mathbf{p}_i;\mathbf{v}_i)\} \tag{B1}$$

and

$$\phi(\mathbf{\Delta}) - \theta(\mathbf{\Delta}) \triangleq E\{I(\mathbf{x}_1-\mathbf{p}_i;\mathbf{v}_i) I(\mathbf{x}_2-\mathbf{p}_i;\mathbf{v}_i)\} \tag{B2}$$

for $\mathbf{x}_1, \mathbf{x}_2 \in [-L, L]^2$. We substitute (8) into (B1) and expand the result into four terms each of which is an expectation with respect to $f_{\mathbf{p}|\mathbf{v}}^{(L)}(\mathbf{P} \mid \mathbf{V}) \mathbf{f}_{\mathbf{v}}^{(\mathbf{L})}(\mathbf{V})$. Evaluation of these expectations for $\mathbf{x}_1, \mathbf{x}_2 \in [-L, L]^2$ yields

$$\begin{aligned}\phi(\mathbf{\Delta}) &= 1 - \int_{-\infty}^{\infty} \frac{2}{[2L+W(\mathbf{V})][2L+H(\mathbf{V})]} A(\mathbf{V}) f_{\mathbf{v}}^{(L)}(\mathbf{V})\, d\mathbf{V} \\ &\quad + \int_{-\infty}^{\infty} \frac{1}{[2L+W(\mathbf{V})][2L+H(\mathbf{V})]} \mathcal{C}(\mathbf{\Delta};\mathbf{V}) f_{\mathbf{v}}^{(L)}(\mathbf{V})\, d\mathbf{V}\end{aligned}$$

where $A(\mathbf{V})$ and $\mathcal{C}(\mathbf{\Delta};\mathbf{V})$ are given by (19) and (21), respectively, for $\mathbf{V} \in \Psi(L)$. Algebraic manipulations yield

$$\phi(\mathbf{\Delta}) = 1 - \frac{2}{(2L)^2}\bar{A}(L) + \frac{1}{(2L)^2}\bar{\mathcal{C}}(\mathbf{\Delta};L) + \frac{1}{(2L)^3}\bar{\gamma}(\mathbf{\Delta},L) \tag{B3}$$

where

$$\bar{\mathcal{C}}(\boldsymbol{\Delta};L)=\int_{-\infty}^{\infty}\mathcal{C}(\boldsymbol{\Delta};\mathbf{V})f_{\mathbf{v}}^{(L)}(\mathbf{V})\,d\mathbf{V}$$

and

$$\bar{\gamma}(\boldsymbol{\Delta},L)=\int_{-\infty}^{\infty}\gamma(\boldsymbol{\Delta},L)f_{\mathbf{v}}^{(L)}(\mathbf{V})\,d\mathbf{V}$$

where

$$\gamma(\boldsymbol{\Delta},L)=2L\frac{2L[W(\mathbf{V})+H(\mathbf{V})]+W(\mathbf{V})H(\mathbf{V})}{[2L+H(\mathbf{V})][2L+W(\mathbf{V})]}\times[2A(\mathbf{V})-\mathcal{C}(\boldsymbol{\Delta};\mathbf{V})].$$

Similarly, the expectation in (B2) is with respect to $f_{\mathbf{p}|\mathbf{v}}^{(L)}(\mathbf{P}\mid\mathbf{V})f_{\mathbf{v}}^{(L)}(\mathbf{V})$. Evaluation of this expectation yields

$$\phi(\boldsymbol{\Delta})-\theta(\boldsymbol{\Delta})=\int_{-\infty}^{\infty}\frac{1}{[2L+W(\mathbf{V})][2L+H(\mathbf{V})]}\times\mathcal{C}(\boldsymbol{\Delta};\mathbf{V})f_{\mathbf{v}}^{(L)}(\mathbf{V})\,d\mathbf{V}$$

which, by algebra, becomes

$$\phi(\boldsymbol{\Delta})-\theta(\boldsymbol{\Delta})=\frac{1}{(2L)^2}\bar{\mathcal{C}}(\boldsymbol{\Delta};L)-\frac{1}{(2L)^3}\bar{\alpha}(\boldsymbol{\Delta},L)\qquad\text{(B4)}$$

where

$$\bar{\alpha}(\boldsymbol{\Delta},L)=2L\int_{-\infty}^{\infty}\frac{2L(W(\mathbf{V})+H(\mathbf{V}))+W(\mathbf{V})H(\mathbf{V})}{(2L+W(\mathbf{V}))(2L+H(\mathbf{V}))}\times\mathcal{C}(\boldsymbol{\Delta};\mathbf{V})f_{\mathbf{v}}^{(L)}(\mathbf{V})\,d\mathbf{V}.$$

We now describe the steps leading to (20). We have

$$0\le\mathcal{C}(\boldsymbol{\Delta};\mathbf{V})\le\mathcal{C}(0;\mathbf{V})=A(\mathbf{V})\le W(\mathbf{V})H(\mathbf{V})$$

so

$$0\le 2A(\mathbf{V})-\mathcal{C}(\boldsymbol{\Delta};\mathbf{V})\le 2W(\mathbf{V})H(\mathbf{V}).$$

Therefore

$$0\le\bar{\gamma}(\boldsymbol{\Delta},L)\le\int_{-\infty}^{\infty}2L\frac{2L[W(\mathbf{V})+H(\mathbf{V})]+W(\mathbf{V})H(\mathbf{V})}{[2L+H(\mathbf{V})][2L+W(\mathbf{V})]}\times 2W(\mathbf{V})H(\mathbf{V})f_{\mathbf{v}}^{(L)}(\mathbf{V})\,d\mathbf{V}.$$

The RHS of the above can be upper bounded by dropping the $H(\mathbf{V})$ and $W(\mathbf{V})$ from the denominator. Application of (A3)–(A5) then yields

$$0\le\bar{\gamma}(\boldsymbol{\Delta},L)\le 2m_{21}(L)+2m_{12}(L)+\frac{1}{L}m_{22}(L).$$

We use the above to bound $\phi(\boldsymbol{\Delta})$ of (B3). If we operate on the resulting bound by $\lambda(2L)^2\log_e$ and apply (A6), we obtain for sufficiently large L

$$\lambda[-2\bar{A}(L)+\bar{\mathcal{C}}(\boldsymbol{\Delta};L)]-\lambda\left[-\frac{1}{L}\bar{A}(L)+\frac{1}{2L}\bar{\mathcal{C}}(\boldsymbol{\Delta};L)\right]^2<\ln\phi^{\lambda(2L)^2}(\boldsymbol{\Delta})<-\lambda 2\bar{A}(L)+\lambda\bar{\mathcal{C}}(\boldsymbol{\Delta};L)+\lambda\frac{1}{2L}\left(2m_{21}(L)+2m_{12}(L)+\frac{1}{L}m_{22}(L)\right).$$

It follows that

$$\lim_{L\to\infty}\phi^{\lambda(2L)^2}(\boldsymbol{\Delta})=e^{-\lambda[2\bar{A}-\bar{\mathcal{C}}(\boldsymbol{\Delta})]}$$

which is used in (16) to obtain (20), where

$$\bar{\mathcal{C}}(\boldsymbol{\Delta})\triangleq\lim_{L\to\infty}\bar{\mathcal{C}}(\boldsymbol{\Delta};L)=\int_{-\infty}^{\infty}\mathcal{C}(\boldsymbol{\Delta};\mathbf{V})p_{\mathbf{v}}(\mathbf{V})\,d\mathbf{V}.$$

The substitution of (B3) and (B4) into the fraction in (16) yields

$$\frac{\phi(\boldsymbol{\Delta})-\theta(\boldsymbol{\Delta})}{1-\phi(\boldsymbol{\Delta})}=\frac{\bar{\mathcal{C}}(\boldsymbol{\Delta};L)-\frac{1}{2L}\bar{\alpha}(\boldsymbol{\Delta},L)}{2\bar{A}(L)-\bar{\mathcal{C}}(\boldsymbol{\Delta};L)-\frac{1}{2L}\bar{\gamma}(\boldsymbol{\Delta},L)}.$$

We bound $\bar{\alpha}(\boldsymbol{\Delta},L)$ by techniques similar to those we used to bound $\bar{\gamma}(\boldsymbol{\Delta},L)$. The result is

$$0\le\bar{\alpha}(\boldsymbol{\Delta},L)\le m_{21}(L)+m_{12}(L)+\frac{1}{2L}m_{22}(L)$$

from which

$$\lim_{L\to\infty}\frac{\phi(\boldsymbol{\Delta})-\theta(\boldsymbol{\Delta})}{1-\phi(\boldsymbol{\Delta})}=\frac{\bar{\mathcal{C}}(\boldsymbol{\Delta})}{2\bar{A}-\bar{\mathcal{C}}(\boldsymbol{\Delta})}$$

which appears in (20).

APPENDIX C

The first-order pdf, $p_s(S;\mathbf{x})$, of image intensity $s(\mathbf{x})$, and the second-order pdf $p_{s_1,s_2}(S_1,S_2;\mathbf{x}_1,\mathbf{x}_2)$ of $s(\mathbf{x}_1)$, $s(\mathbf{x_2})$ can be easily found in terms of the first and second-order pdf's of background intensity, $b(\mathbf{x})$, and object-image intensity, $I(\mathbf{x})$. We assume that $I(\mathbf{x})$ is second-order stationary in the strict sense.

For the first-order pdf of $s(\mathbf{x})$, we have

$$\begin{aligned}p_s(S;\mathbf{x})&=p_s(S;\mathbf{x}\mid B(\mathbf{x}))\Pr\{B(\mathbf{x})\}\\&\quad+p_s(S;\mathbf{x}\mid O(\mathbf{x}))\Pr\{O(\mathbf{x})\}\\&=p_b(S;\mathbf{x})P_b(0)+p_I(S)P_o(0)\end{aligned}\qquad\text{(C1)}$$

where $P_b(0)$ and $P_o(0)$ follow from (28)–(29). It follows from (C1) that $p_s(S;\mathbf{x})$ is a mixture density. The derivation of the second-order pdf is longer, but nearly as simple:

$$\begin{aligned}&p_{s_1,s_2}(S_1,S_2;\mathbf{x}_1,\mathbf{x}_2)\\&\quad=p_{s_1,s_2}(S_1,S_2;\mathbf{x}_1,\mathbf{x}_2\mid O(\mathbf{x}_1)O(\mathbf{x}_2))\Pr\{O(\mathbf{x}_1)O(\mathbf{x}_2)\}\\&\qquad+p_{s_1,s_2}(S_1,S_2;\mathbf{x}_1,\mathbf{x}_2\mid O(\mathbf{x}_1)B(\mathbf{x}_2))\Pr\{O(\mathbf{x}_1)B(\mathbf{x}_2)\}\\&\qquad+p_{s_1,s_2}(S_1,S_2;\mathbf{x}_1,\mathbf{x}_2\mid B(\mathbf{x}_1)O(\mathbf{x}_2))\Pr\{B(\mathbf{x}_1)O(\mathbf{x}_2)\}\\&\qquad+p_{s_1,s_2}(S_1,S_2;\mathbf{x}_1,\mathbf{x}_2\mid B(\mathbf{x}_1)B(\mathbf{x}_2))\Pr\{B(\mathbf{x}_1)B(\mathbf{x}_2)\}.\end{aligned}\qquad\text{(C2)}$$

To evaluate the first term on the RHS of (C2), we form the partition

$$O(\mathbf{x}_1)O(\mathbf{x}_2)=O(\mathbf{x}_1,\mathbf{x}_2)\cup D(\mathbf{x}_1,\mathbf{x}_2)\qquad\text{(C3)}$$

where we define the event $D(\mathbf{x}_1,\mathbf{x}_2)=\{$parts of different objects are visible at $\mathbf{x}_1$ and $\mathbf{x}_2\}$. By using (C3), we can write the first term of (C2) as

$$\begin{aligned}&p_{s_1,s_2}(S_1,S_2;\mathbf{x}_1,\mathbf{x}_2\mid O(\mathbf{x}_1)O(\mathbf{x}_2))\Pr\{O(\mathbf{x}_1)O(\mathbf{x}_2)\}\\&\quad=p_{s_1,s_2}(S_1,S_2;\mathbf{x}_1,\mathbf{x}_2\mid O(\mathbf{x}_1,\mathbf{x}_2))\Pr\{O(\mathbf{x}_1,\mathbf{x}_2)\}\\&\qquad+p_{s_1,s_2}(S_1,S_2;\mathbf{x}_1,\mathbf{x}_2\mid D(\mathbf{x}_1,\mathbf{x}_2))\Pr\{D(\mathbf{x}_1,\mathbf{x}_2)\}\\&\quad=p_{I_1,I_2}(S_1,S_2;\boldsymbol{\Delta})P_o(\boldsymbol{\Delta})\\&\qquad+p_I(S_1;\mathbf{x}_1)p_I(S_2;\mathbf{x}_2)\Pr\{D(\mathbf{x}_1,\mathbf{x}_2)\}\end{aligned}\qquad\text{(C4)}$$

where $\Pr\{D(\mathbf{x}_1,\mathbf{x}_2)\} = \Pr\{O(\mathbf{x}_1)O(\mathbf{x}_2)\} - \Pr\{O(\mathbf{x}_1,\mathbf{x}_2)\}$. The substitution of (C4) into (C2) and straightforward evaluation of the remaining terms of (C2) yields

$$\begin{aligned} p_{s_1,s_2}(S_1,S_2;\mathbf{x}_1,\mathbf{x}_2) &= p_{I_1,I_2}(S_1,S_2;\boldsymbol{\Delta})P_o(\boldsymbol{\Delta}) \\ &\quad + p_I(S_1;\mathbf{x}_1)p_I(S_2;\mathbf{x}_2)\Pr\{D(\mathbf{x}_1,\mathbf{x}_2)\} \\ &\quad + p_I(S_1)p_b(S_2;\mathbf{x})p_I(S)\Pr\{O(\mathbf{x}_1)B(\mathbf{x}_2)\} \\ &\quad + p_I(S_2)p_b(S_1;\mathbf{x})p_I(S)\Pr\{B(\mathbf{x}_1)O(\mathbf{x}_2)\} \\ &\quad + p_{b_1,b_2}(S_1,S_2;\mathbf{x}_1,\mathbf{x}_2)\Pr\{B(\mathbf{x}_1)B(\mathbf{x}_2)\} \end{aligned} \quad \text{(C5)}$$

which, like (C1), is a mixture pdf. The probabilities $(\Pr)$ appearing in (C5) are easily found using the expressions developed in this paper.

As an example, consider the occluding disks of Section III, Example 1. Here, the last three terms on the RHS of (C5) vanish because $\lambda\bar{A} \gg 1$. Since $I(\mathbf{x})$ is a random constant, the first two terms on the RHS of (C5) simplify, and (C5) becomes

$$\begin{aligned} p_{s_1,s_2}(S_1,S_2;\mathbf{x}_1,\mathbf{x}_2) &= \delta(S_2-S_1)p_I(S_1)\left\{\frac{\bar{C}_n(\boldsymbol{\Delta})}{2-\bar{C}_n(\boldsymbol{\Delta})}\right\} \\ &\quad + p_I(S_1)p_I(S_2)\left\{\frac{2-2\bar{C}_n(\boldsymbol{\Delta})}{2-\bar{C}_n(\boldsymbol{\Delta})}\right\}. \end{aligned} \quad \text{(C6)}$$

ACKNOWLEDGMENT

The authors gratefully acknowledge Prof. S. Trimble whose comments led to improvements in Appendixes A and B.

REFERENCES

[1] J. Aitchison and J. A. C. Brown, *The Lognormal Distribution*. Cambridge, U.K.: Cambridge Univ. Press, 1976.
[2] A. J. Baddeley and M. N. M. van Lieshout, "ICM for object recognition," in *Proc. 10th Symp. Computational Statistics*. Heldeberg, Germany: Physica-Verlag, 1992, vol. 2, pp. 271–286.
[3] L. Crow and K. Shimizu (Ed.), *Lognormal Distributions*. New York: Marcel Dekker, 1988.
[4] L. E. Franks, "A Model for the random video process," *Bell Syst. Tech. J.*, vol. 45, pp. 609–630, 1966.
[5] A. Habibi and P. A. Wintz, "Image coding by linear transformation and block quantization," *IEEE Trans. Commun. Technol.*, vol. 19, pp. 50–62, 1971.
[6] E. T. Jaynes, "Prior probabilities," *IEEE Trans. Syst. Sci. Cybern.*, vol. SSC-4, 1968.
[7] A. K. Jain, "Advances in mathematical models for image processing," *Proc. IEEE*, May 1981, vol. 69, pp. 502–528.
[8] E. R. Kretzmer, "Statistics of television signals," *Bell Syst. Tech. J.*, vol. 31, pp. 751–763, 1952.
[9] G. Matheron, *Elements pour une Théorie des Milieux Poreux*. Paris, France: Masson, 1967.
[10] G. Matheron, Schéma booléen séquentiel de partitions aléatories, Int. Rep., Ctr. de Morphol. Math., Fontainebleau, France, 1968.
[11] J. W. Modestino, R. W. Fries, and A. L. Vickers, "Stochastic image models generated by random tessallations of the plane," *Image Modeling*, A. Rosenfeld, Ed. New York: Academic, pp. 301–325, 1981.
[12] M. Ritterman, "An application of autocorrelation theory to TV," *Sylvania Technologist*, pp. 70–75, 1952.
[13] W. F. Schreiber, "Fundamentals of electronic imaging systems, some aspects of image processing," in *Springer Series in Information Sciences*, 3rd ed. Berlin, Germany: Springer-Verlag, 1993.
[14] J. Serra, "The boolean model and random sets," *Image Modeling*, A. Rosenfeld, Ed. New York: Academic, pp. 343–370, 1981.
[15] R. M. Shah, "Investigation of autocovariance models of images for transform coding," Master's thesis, Univ. Missouri-Rolla, 1996.
[16] J. A. Stuller and B. Kurz, "Two-dimensional Markov representations of sampled images," *IEEE Trans. Commun.*, pp. 1148–1152, Oct. 1976.
[17] J. A. Stuller, "A Two-dimensional image model based on occlusion and maximum entropy," in *Proc. 29th Asilomar Conf. Signals, Systems and Computers*, Oct. 29–Nov. 1, 1995.
[18] J. M. Tenenbaum, M. A. Fischler, and H. B. Barrow, "Scene modeling: A structural basis for image description," *Image Modeling*, A. Rosenfeld, Ed. New York: Academic, pp. 371–389, 1981.
[19] J. W. Woods, "Two-dimensional discrete Markov fields," *IEEE Trans. Inform. Theory*, vol. IT-18, pp. 232–240, Mar. 1972.

John A. Stuller was born in Norwalk, CT, in 1941. He received the B.Sc. degree from the Massachusetts Institute of Technology, Cambridge, in 1963, the M.Sc. degree from the University of Southern California, Los Angeles, in 1967, and the Ph.D. degree from the University of Connecticut, Storrs, in 1971, all in electrical engineering.

He has held staff positions with Northrop Nortronics, Palos Verdes, CA, TRW Systems Group, Redondo Beach, CA, Perkin Elmer Corporation, Danbury, CT, and Bell Laboratories, Holmdel, NJ. From 1971 to 1977 he was a member of the faculty of the University of New Brunswick, Fredericton, N.B., Canada. From August 1985 to August 1986 he was on leave from the University of Missouri-Rolla at the Naval Underwater Systems Center, New London, CT. He is presently a Professor of Electrical Engineering at the University of Missouri-Rolla.

Rahul Shah was born in Bilaspur (MP), India, in 1970. He received the B.Eng. (electronics) degree from the University of Bombay, India, in 1993, and the M.S. degree in electrical engineering from the University of Missouri-Rolla in 1996.

He has been an R.F. Engineer at Mobile Systems International, Inc. He is currently a Systems Test Engineer at Qualcomm, Inc., San Diego, CA. His areas of interest include data compression, wireless, and satellite communications.